

# Physical mechanisms of timing jitter in photon detection by current-carrying superconducting nanowires

Mariia Sidorova, Alexej Semenov, and Heinz-Wilhelm Hübers  
*DLR Institute of optical systems, Rutherfordstrasse 2, 12489 Berlin, Germany*

Ilya Charaev, Artem Kuzmin, Steffen Doerner, and Michael Siegel  
*Institut für Mikro- und Nanoelektronische Systeme (IMS), Karlsruher Institut für Technologie (KIT),  
Hertzstrasse 16, 76187 Karlsruhe, Germany*

(Received 19 July 2017; revised manuscript received 16 October 2017; published 6 November 2017)

We studied timing jitter in the appearance of photon counts in meandering nanowires with different fractional amount of bends. Intrinsic timing jitter, which is the probability density function of the random time delay between photon absorption in current-carrying superconducting nanowire and appearance of the normal domain, reveals two different underlying physical mechanisms. In the deterministic regime, which is realized at large photon energies and large currents, jitter is controlled by position-dependent detection threshold in straight parts of meanders. It decreases with the increase in the current. At small photon energies, jitter increases and its current dependence disappears. In this probabilistic regime jitter is controlled by Poisson process in that magnetic vortices jump randomly across the wire in areas adjacent to the bends.

DOI: [10.1103/PhysRevB.96.184504](https://doi.org/10.1103/PhysRevB.96.184504)

## I. INTRODUCTION

In the interaction between photons and matter, conversion of photon energy to excitation in the electronic spectrum and further to measurable change of any of macroscopic parameters is the subject of statistical fluctuations. These fluctuations randomize the time delay between photon absorption and the appearance of the change in the parameter of interest. Revealing physical mechanisms, which constitute the delay, improves our understanding of light-matter interaction. In photonic applications, random time delay causes timing jitter in the appearance of the voltage transient, which a photon detector produces on each detection event. The measure of the timing jitter is the width of the statistical distribution in the arrival times of voltage transients with respect to the corresponding photon absorption times. Nowadays, one of the actively developing detector technologies is superconducting nanowire single-photon detectors (SNSPDs). Although impressive progress has been achieved during recent decades in SNSPD technology, performance of these detectors is still improving. Timing jitter is one of the important SNSPD metrics. It limits the accuracy of measurements of photon arrival times and is crucial for SNSPD application in laser ranging, communication technologies, or time-resolved correlation measurements. Although diminishing timing jitter may greatly extend application field of SNSPDs, such progress is hardly possible without understanding how different physical mechanisms contribute to the jitter magnitude.

During the past decade, many groups have reported on small timing jitter in SNSPDs. However, measurements were done with different detector layouts and electronics that hamper direct comparison. System jitter with full width at half maximum (FWHM) as low as 18 ps has been demonstrated for SNSPD based on NbN [1,2]. It has been realized that electronic noise severely enhances system jitter and causes its current dependence. By subtracting the noise contribution, one obtains jitter inherent in the detector, which is called intrinsic jitter. It was found that the intrinsic jitter increases in

nanowires with smaller thickness and larger kinetic inductance per unit length [3]. Furthermore, the jitter increases with the size of the detector [4,5] and is less for the central part of the detector area as compared to peripherals [6]. Although low jitter is a challenge, it becomes attractive only in conjunction with the practical values of the detection efficiency and maximum count rate. Since the size of the detector affects these two metrics differently, it stays necessarily in the list of trade-off parameters. Jitter increases in nanowires from superconducting films with low transition temperature. For nanowires from WSi [7] and MoSi [8], jitter is almost one order of magnitude larger than in nanowires from NbN.

While instrumental aspects of the system timing jitter have been thoroughly discussed, physical mechanisms of the intrinsic jitter remain largely unclear. Revealing those mechanisms should give the answer how to decrease jitter magnitude and what the limit is. For WSi, Fano fluctuations were shown to broaden the decay of the photon detection efficiency with the decrease of the current through the nanowire [9]. They should also affect the time delay between photon absorption and the emergence of the resistive state. Whether this mechanism may affect jitter in NbN nanowires is not clear. Several sequential processes constitute the delay between photon absorption and appearance of the normal domain in the nanowire. These processes are down conversion of the photon energy in electronic excitations and growing of the hot-spot, vortex crossing and formation of the normal domain. For NbN, delay time of the resistive state formation after absorption of the photon was estimated to exceed 65 ps [10]. It has been shown that the formation time may depend on the film thickness via escape of nonthermal phonons to the substrate [11]. Recent publication [12] has reported on the current dependence of the lifetime of the hot-spot in NbN in the range 20–45 ps. Spread in the traveling time of a magnetic vortex across the nanowire has been analyzed theoretically [13]. For NbN, the mean value of 9 ps and the jitter less than

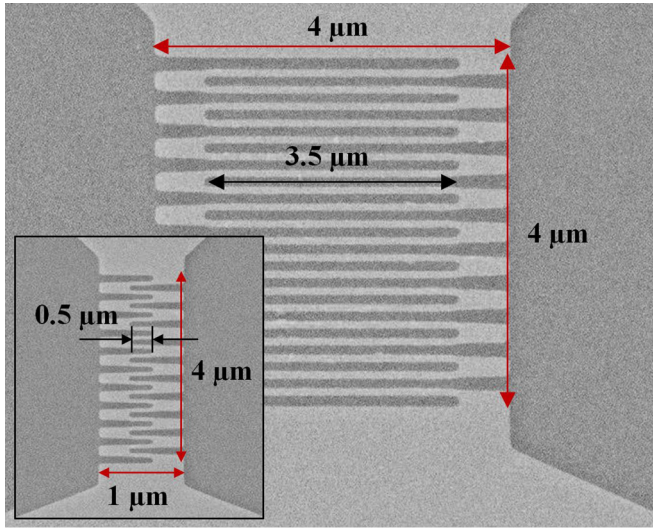


FIG. 1. Images of the largest and the smallest (inset) meanders obtained with a scanning electron microscope. The size of the largest meander is  $4 \times 4 \mu\text{m}^2$ ; the length of straight wires between bends is  $3.5 \mu\text{m}$ . The size of the smallest meander is  $4 \times 1 \mu\text{m}^2$ ; the length of straight wires between bends is  $0.5 \mu\text{m}$ .

2 ps were predicted. However, the time delay itself does not explicitly set the magnitude of the jitter.

Here we report on the study of the intrinsic jitter in differently shaped NbN meanders at two wavelengths providing different detection regimes. Our meanders contain different relative amount of straight wires and fixed number of bends. Along with the transmission line approach, a set of different layouts allows us to evaluate local and geometric contributions to the jitter. Furthermore, we separate contributions from straight nanowires and bends. We show that jitter statistics and its current dependencies change with the wavelength and differ between straight wires and bends. We discuss mechanisms constituting jitter and propose simplified physical models which provide good quantitative description of our experimental findings.

## II. EXPERIMENT

### A. Sample preparation

Our meanders were drawn by electron beam lithography from a 5-nm-thick NbN superconducting film deposited on

$\text{Al}_2\text{O}_3$  substrate. Nanowires had a width of 90 nm and a filling factor of 50% (Fig. 1). The nanowire was connected to contact pads shortening a coplanar transmission line. We studied meanders having different sizes:  $4 \times 4$ ,  $4 \times 3$ ,  $4 \times 2$ , and  $4 \times 1 \mu\text{m}^2$  but the same number of bends. Shape and size of bends were identical for all meanders as well as within one meander. Correspondingly, the length of straight wires between bends was 3.5, 2.5, 1.5, and  $0.5 \mu\text{m}$ . Hence, in the largest meander (Fig. 1), the nanowire consists mostly from straight parts while in the smallest meander (inset to Fig. 1) bends dominate the total length of the nanowire. Transport measurements at 4.2 K showed similarity in the values of critical currents  $37.6\text{--}41.1 \mu\text{A}$  and superconducting transition temperatures  $13.05\text{--}13.35 \text{ K}$  of different meanders. Normal square resistance of the original films was  $243 \text{ Ohm/square}$  at 25 K.

### B. Experimental approach

Jitter measurements were carried out at 4.2 K and two wavelengths 800 and 1560 nm. Meanders were uniformly illuminated by laser pulses with sub-picosecond duration with a repetition rate between 80 and 100 MHz. Meanders were biased via a bias-tee with a DC current supplied by a battery-powered electronics. Voltage transients generated on counting events were amplified at room temperature with low noise amplifier, which had the bandpass from 100 MHz to 8 GHz and the noise level of 1.4 dB, and acquired by a sampling oscilloscope with the bandwidth of 50 GHz. The oscilloscope was triggered by electrical pulses from a fast photodiode which was illuminated by laser pulses [Fig. 2(a)]. Electric cables with the total length of approximately 4 m introduced an instrumental delay of 20 ns in the appearance of the voltage transient at the oscilloscope. A typical voltage transient obtained by sampling many counting events is shown in Fig. 2(b). To build a histogram, we accumulated more than  $10^4$  points inside an acquisition window on the rising edge of the voltage transient [shown by the rectangle in Fig. 2(b)]. We associated the arrival time of the transient with the time when the points from this transient appear within the window. The distribution of arrival times (histogram) was then computed with the time bin less than 0.3 ps. The histogram represents probability density function (PDF) of the arrival time which is considered to be a random continuous variable. Extracted

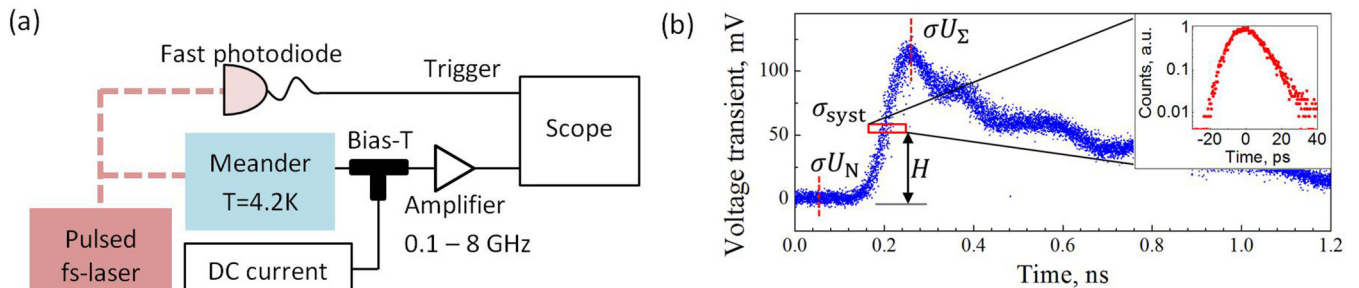


FIG. 2. (a) Schematics of the setup for jitter measurements at 800 and 1560 nm. (b) Voltage transient recorded by the 50 GHz sampling oscilloscope. Points occurring within the rectangle window at the level  $H$  are used to build statistical distribution of arrival times shown in the inset. Dotted lines show locations where the vertical distributions of sampling points were additionally measured.  $\sigma U_\Sigma$ ,  $\sigma U_N$ , and  $\sigma_{\text{syst}}$  denote corresponding standard deviations.

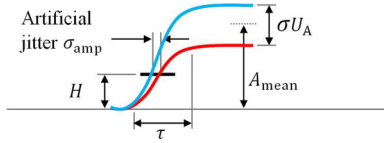


FIG. 3. Artificial jitter  $\sigma_{\text{amp}}$  due to the difference in amplitudes of two pulses arriving at the same time.

PDFs [one of them exemplarily shown in the inset in Fig. 2(b)] typically had a non-Gaussian profile with an exponential tail extended to larger arrival times. Formally defined standard deviation for such asymmetric PDF does not necessarily correlates with the width of the histogram. To circumvent this problem and increase the accuracy, we fit histograms with Eq. (4) and measured the full width at half maximum (FWHM) of best fit curves. Reasons for using Eq. (4) to fit experimental histograms are discussed below. We further define the standard deviation  $\sigma_{\text{sys}}$  as the  $1/2.35$  part of the measured FWHM value. Hereafter we will use this standard deviation as the measure of timing jitter. We have found that the system jitter,  $\sigma_{\text{sys}}$ , was noticeably affected by the noise in the electrical network, fluctuations in the transient amplitude, and the level,  $H$  [Fig. 2(b)] where the acquisition window was positioned. In the experiment reported here, we set acquisition window at the half of the amplitude of the corresponding voltage transient.

We estimate instrumental contribution to the measured jitter by substituting the meander with another fast photodiode and measuring histograms with different optical fibers between the laser and this photodiode. All instrumental histograms had Gaussian form and were fully symmetric down to the level of  $10^{-3}$  from the distribution maximum. The instrumental jitter  $\sigma_{\text{instr}}$  was less than 1.5 ps for illumination via open beam and increased to 2 or 1.7 ps when light was delivered to the photodiode by two meters of multimode fiber or three meters of single mode fiber, respectively. Noise contribution to the system jitter was estimated [3,14] as  $\sigma_{\text{noise}} = \sigma U_N \cdot \tau / A_{\text{mean}}$ , where  $A_{\text{mean}}$  is the mean transient amplitude,  $\tau$  is duration of the rising edge of the voltage transient and  $\sigma U_N$  is standard deviation extracted from the height of histogram of sampling points at the base line [Fig. 2(b)].

It was found that SNSPDs pulses exhibit amplitude fluctuations [15]. These fluctuations cause additional jitter. Figure 3(a) shows schematically two voltage pulses with different amplitudes arriving at the same time. If one builds up time distribution of sampling points at the level  $H$ , any difference in the amplitudes will broaden this distribution producing artificial jitter,  $\sigma_{\text{amp}}$ . Simple math results in the following connection between  $\sigma_{\text{amp}}$  and the standard deviation  $\sigma U_A$  in the distribution of transient amplitudes,

$$\sigma_{\text{amp}} = \sigma U_A \frac{\tau H}{A_{\text{mean}}^2}, \quad (1)$$

where  $\sigma U_A = \sqrt{\sigma U_{\Sigma}^2 - \sigma U_N^2}$ , and  $\sigma U_{\Sigma}$  is the standard deviation in the vertical distribution of point heights measured as the top of the voltage transient [Fig. 2(b)].

We found that electrical noise and amplitude fluctuations had almost Gaussian distributions. Further assuming that they are statistically independent, we obtained the standard

deviation in the intrinsic jitter as

$$\sigma_{\text{int}} = \sqrt{\sigma_{\text{sys}}^2 - (\sigma_{\text{noise}}^2 + \sigma_{\text{amp}}^2 + \sigma_{\text{instr}}^2)}. \quad (2)$$

In the data reported below, the noise contribution typically remained less than one quarter of the measured system jitter and introduced only a moderate error in the computed intrinsic jitter. In our experimental approach with single readout line, geometric jitter is associated with different traveling times of current steps from different absorption sites to an arbitrary reference plane in the coplanar line. Appearance of the normal domain and propagation of the current steps are sequential independent events. Although the shape of experimental histograms (PDFs) differs from the normal distributions, we suppose that the dispersion in the intrinsic PDF is the sum of dispersions in the partial PDFs associated with the appearance of the normal domain and with the travelling time of current steps. Since statistics in the appearance of the normal domain is inherent to the absorption site, we will hereafter denote the corresponding local standard deviation as  $\sigma_{\text{loc}}$  and the geometric contribution as  $\sigma_{\text{geom}}$ . The standard deviation in the intrinsic jitter can be then presented as

$$\sigma_{\text{int}} = \sqrt{\sigma_{\text{loc}}^2 + \sigma_{\text{geom}}^2}. \quad (3)$$

We shall note here that common output in our experimental approach is expected to eliminate geometric jitter. One end of the meandering nanowire of the total length  $L$  is connected to the ground plane of the coplanar line and another one to the central strip of the line. Let us define the reference plane at this second end. When a photon initiates counting event at the distance  $x$  along the nanowire from the reference plane, two current steps start to propagate to the opposite directions from the absorption site. One step arrives at the reference plane after the time  $t_1 = x/v$  where  $v \approx 12 \mu\text{m}/\text{ps}$  is the propagation velocity of the current step along the superconducting nanowire [16]. Another step propagates till the shorted end of the nanowire and travels further to the reference plane via the outer ground strips of the coplanar line. This second step arrives at the reference plane after the time  $t_2 = (L - x)/v + a/v^*$ , where  $v^* \approx 140 \mu\text{m}/\text{ps}$  is the propagation velocity of the current step in the coplanar line on sapphire and  $a = 4 \mu\text{m}$  is the outer size of the meander. The arrival time of the ‘‘center of mass’’ of two current steps  $(t_1 + t_2)/2 = L/v + a/v^*$  does not depend on  $x$  and hence does not suffer jitter. Here we neglected mutual reflections of current steps at both ends of the nanowire due to impedance mismatch. For our largest meander with  $L = 70 \mu\text{m}$ , the maximum difference between arrival times of two current steps at the reference plane,  $t_1 - t_2 \approx 5.5$  ps, is much less than the intrinsic transient time of the amplifier (42 ps). Therefore the amplifier does not resolve two current steps and outputs only one voltage transient (Fig. 2b) for single detection event. The central point  $H = 0.5 A_{\text{mean}}$  of the rising edge of the transient occurs at the delay time which does not depend on  $x$ . Geometric jitter may appear in this configuration only if the damping and/or dispersion are different in the nanowire and in the ground plane. Hence, we expect small geometric jitter if any to be present in our experimental data.

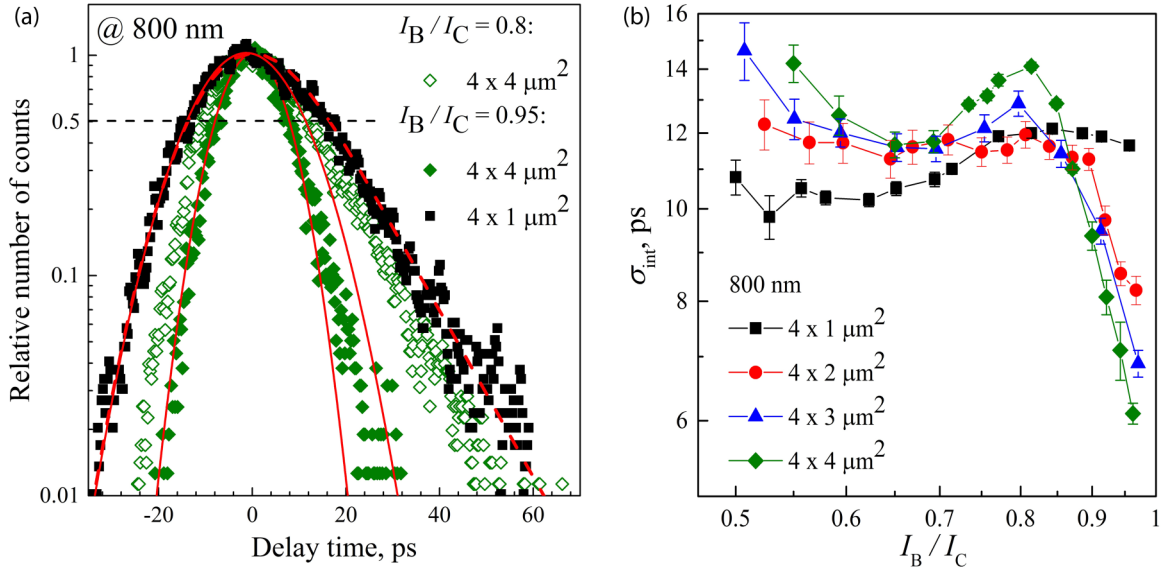


FIG. 4. (a) Histograms (PDFs) of the delay time for the meander  $4 \times 4 \mu\text{m}^2$  and  $4 \times 1 \mu\text{m}^2$  at currents  $0.95 I_C$  (closed symbols) and for the meander  $4 \times 4 \mu\text{m}^2$  at the current  $0.8 I_C$  (open symbols). Data were obtained at 4.2 K and the wavelength 800 nm. Horizontal dashed line marks the level where FWHM were defined. Solid lines show Gaussian fits to the left parts of histograms. Dashed line shows the best fit of the PDF for the smaller meander with Eq. (4). (b) Standard deviation in the intrinsic jitter as function of bias current for four studied meanders. The error bars denote cumulative uncertainties which arise from fitting PDFs with Eq. (4) and computing  $\sigma_{\text{int}}$  with Eq. (2). Lines are to guide the eyes.

### III. RESULTS

#### A. Excitation wavelength 800 nm

Experimental histograms, i.e., relative numbers of photon counts per time-bin are shown in Fig. 4(a) for two meanders as function of the delay time. The data were acquired at the wavelength 800 nm and at two bias currents  $I_B = 0.95 I_C$  and  $I_B = 0.8 I_C$ , where  $I_C$  is the experimental critical current. As discussed above, the data represent probability distribution functions of arrival times. Since the exact delay time between the photon arrival and the transient appearance is not known, the maxima of PDFs were assigned zero delay values. We are not going to discuss here the true probability of the photon detection. Therefore, PDFs are normalized to one at their maxima. In the semi-logarithmic scale, asymmetry in PDFs is clearly seen. Such deviation from normal distribution is typical for meanders and was observed by a number of groups [1,2,6,14,17]. Our data show that the asymmetry is more pronounced for the meander with smaller relative amount of straight wires. Decrease in the bias current much stronger affects the dispersion at large delays than at small delays, although the shapes remain almost unchanged.

All measured PDFs have Gaussian shapes at small delays and drop linearly (in semilogarithmic scale) with time at large delays. Linear decrease of the PDFs at large delays evidences that the delay time includes a sequential stage with exponential distribution of probability density function. The asymmetry rules out Gaussian fit [solid lines in Fig. 4(a)] as a valid instrument of finding standard deviation in PDFs. Instead, we fitted measured histograms with Eq. (4) and defined system jitter  $\sigma_{\text{sys}}$  as  $1/2.35$  part of FWHM for each fitting curve. To obtain intrinsic jitter, we subtracted from  $\sigma_{\text{sys}}$  the instrumental contribution as well as the contributions from amplitude fluctuations and electric noise according to Eqs. (1)–(3). We

have found that  $\sigma_{\text{amp}}$  and  $\sigma_{\text{noise}}$  significantly affect  $\sigma_{\text{sys}}$  only at small bias currents. Furthermore, contribution to the intrinsic jitter due to amplitude fluctuations is much less than the noise contribution. They become comparable only at small bias currents. For instance, for the meander  $4 \times 1 \mu\text{m}^2$  at  $0.95 I_C$  the value of  $(\sigma_{\text{noise}}^2 + \sigma_{\text{amp}}^2)^{1/2} \approx 2.6$  ps against  $\sigma_{\text{sys}} \approx 12.2$  ps. However, at the bias current  $0.6 I_C$  these values are  $\approx 8.7$  ps and  $\approx 12.7$  ps, respectively. Uncertainty in  $\sigma_{\text{sys}}$  at large currents arises due to the fitting procedure. Instrumental contribution to  $\sigma_{\text{sys}}$  was negligibly small and current independent. Since the instrumental and the noise contributions were symmetric and had Gaussian profiles, we suppose that the observed asymmetry is inherent in photon detection in meanders.

The intrinsic jitter is shown in Fig. 4(b) as function of the bias current for four studied meanders. At small currents, the jitter increases with an increase in the total length of straight wires. Contrarily, the intrinsic jitter turns to have the smallest value for the largest meander when the bias current approaches the critical current. By measuring the dependencies of the count rate on the light intensity and the bias current, we verified that at currents less than  $0.7 I_C$  meanders undergo the transition to multi-photon detection regime. Jitter for multiphoton detection goes beyond the scope of the present study. Here we will discuss results exclusively at large bias currents.

#### B. Excitation wavelength 1560 nm

Histograms acquired at 1560 nm for two different meanders at  $I_B = 0.95 I_C$  are shown in Fig. 5(a). At this wavelength histograms were also asymmetric but the degree of asymmetry was larger than in histograms acquired at 800 nm. Differently to the wavelength 800 nm, all meanders demonstrated the

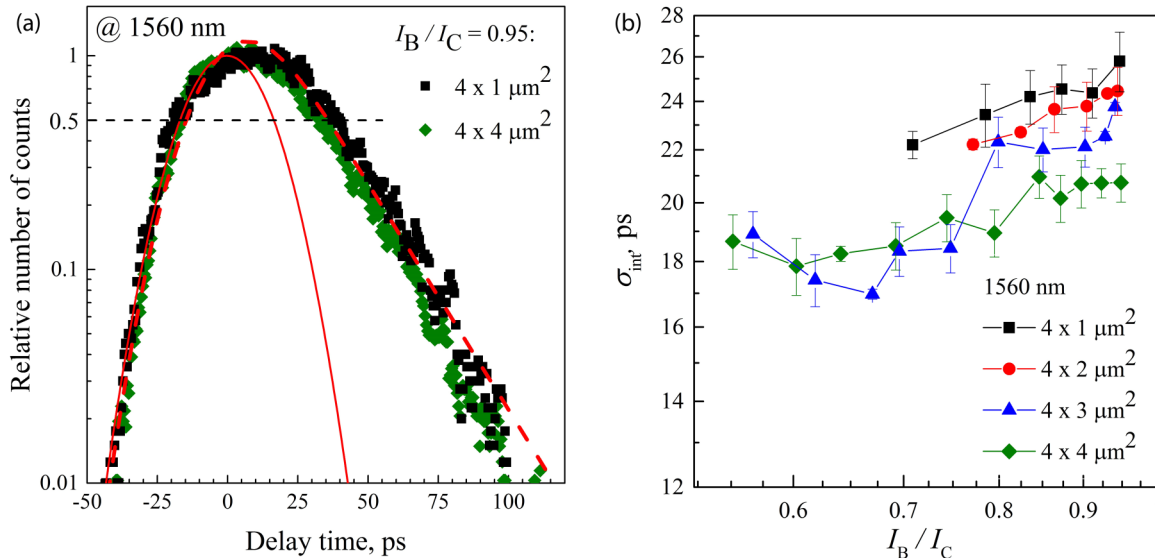


FIG. 5. (a) Histograms (PDFs) of the delay time at the current  $0.95I_C$  for the meanders  $4 \times 4 \mu\text{m}^2$  (rhombs) and for the meander  $4 \times 1 \mu\text{m}^2$  (squares). Data were obtained at 4.2 K and the wavelength 1560 nm. Horizontal dashed line marks the level where FWHM were defined. Solid line shows Gaussian fit to the left parts of the histograms. Dashed line shows the best fit of the PDF with Eq. (4) for the meander  $4 \times 1 \mu\text{m}^2$ . (b) Standard deviation in the intrinsic jitter as function of bias current for four studied meanders. The error bars denote cumulative uncertainties which arise from fitting PDFs with Eq. (4) and computing  $\sigma_{\text{intr}}$  with Eq. (2). Lines are to guide the eyes.

same dispersion at small delays. At large delays, dispersion increases with the decrease of the meander size. For all meanders, intrinsic jitter monotonically increases with the bias current [Fig. 5(b)]. Due to low detection efficiency at 1560 nm, specifically for two smaller meanders, the required integration time becomes larger than long-term stability time of the setup. As the result, the instantaneous dispersion first decreases with the increase in the integration time but starts to increase when the integration time exceeds the long-term stability time. Therefore, we were not able to get reliable data for small meanders at small bias currents. Anyway, data at currents less than  $0.7I_C$  would not be discussed here since multiphoton detection dominates at small currents.

#### IV. DISCUSSION

Before going into discussion of experimental data we would like to sketch the detection scenario and mark physical processes which build up the delay between photon absorption and emergence of the normal conducting domain in the nanowire. In a superconducting nanowire, photon counting event is a sequence of several elementary events (stages), which are (i) photon absorption, (ii) thermalization, i.e., energy transfer from the absorbed photon to electrons in the nanowire, (iii) growing and disappearance of the hot-spot, (iv) emergence of the normal domain, and (v) propagation of two current steps through the nanowire and through the nanowire and ground plane, respectively, to the input of the common transmission line. It is worth noting that in NbN characteristic times of stages (ii) and (iii) are close and therefore these stages cannot be clearly distinguished. Hereafter, we use the term hot-spot to denote nonequilibrium distribution of electrons (quasiparticles) around the absorption site of the photon. Physically, a normal core in the hot-spot may appear or may not appear depending on the energy of the absorbed photon

and the current. Anyway, to simplify the model describing jitter, we will define the size of the hot-spot via geometric criteria used in the model of diffusive normal-core [18]. All stages listed above contribute to the intrinsic jitter while local jitter inheres in the photon detection itself and accumulates contributions from only first four stages.

With the proper polarization, absorbance is uniform over the nanowire and hardly contributes extra randomness to the delay time. Thermalization (ii) is the subject of Fano fluctuations [19]. They randomize the amount of energy transferred from the photon to electrons and, consequently, the size of the hot-spot when it is defined at the fixed delay time or the delay time in the appearance of the hot-spot with the fixed size. Given that the rate of dark counts is sufficiently small, the hot-spot (iii) opens the time window for emergence of the normal domain. Following the location of the absorption site, normal domain emerges either in the straight portion of the nanowire or in the bend. These are two mutually exclusive events for which total PDF is a sum of individual PDFs [20] weighted with relative areas covered by bends and straights.

It is commonly accepted [21–23] that the normal domain emerges [stage (iv)] immediately after a magnetic vortex crosses the nanowire. Vortex crossing randomizes the total delay time. Corresponding PDFs include contributions from the random start time of the crossing and from the random flight time of the vortex across the nanowire [13]. While the flight time is almost entirely controlled by the current through the nanowire, the mean start time depends on the instant value of the energy barrier for vortex entry and hence on the photon energy. Opening of the time window by the hot-spot and vortex crossing are independent sequential events. PDF of the composite event is the integral of the product of elementary PDFs [20].

Vortex crossing occurs either in the deterministic or in the probabilistic regime. Which of them is realized at

particular absorption site depends on the operation parameters: temperature, current, and photon energy. Transition between two regimes is controlled by the position dependence of the detection probability [24] and, correspondingly, of the local detection current [25]. The local detection current is the smallest current through the nanowire that is required to achieve 100% detection probability (probability of vortex crossing) for photon absorbed at this particular location [25,26]. For bias currents larger than the local value of the detection current at any location in the nanowire, it undergoes deterministic detection regime. In this regime the energy barrier for vortex entry is completely suppressed and the rate of photon counts saturates as function of wavelength or current [22]. When the current is smaller than the smallest detection current, the nanowire exhibits probabilistic detection regime. This means that the probability of vortex crossing at the absorption site is less than one and depends on the instant value of the energy barrier for vortex entry. In this regime, the rate of photon counts decreases rapidly when the current of photon energy decreases [21,22]. Blurred transition between two regimes as function of current or wavelength occurs around the cut-off wavelength [21,27] and corresponds to separation of the wire into two parts undergoing different detection regimes [28]. In a meander, straight wires and bends may exhibit different detection regimes [29] that additionally blur the transition. Vortex crossing in the presence of the energy barrier is a Poisson process [20,30] in that the start time of a single crossing obeys the same statistics as, e.g., nuclear decay and is described by an exponential PDF.

Vortex crossing of any kind generates the normal domain and, consequently, two current steps which propagate to opposite directions from the absorption site [stage (v)]. Generally, the propagation times of two steps are different for different absorption sites. This introduces geometric jitter. In the framework of the transmission-line approach, geometric jitter is controlled by the length of nanowire, its kinetic inductance, and the layout which define jointly propagation velocity of electrical signal along the nanowire (Table I). Experimental approach which allows for direct measurements of the geometric jitter is called differential technique [4]. In this technique, arrival times of two electrical pulses originating from the same count event are measured independently at two ends of a nanowire. As it has been discussed above (Sec. II B), readout with only one common line allows one to eliminate geometric jitter to a large extent.

Table I summarizes different factors affecting components of intrinsic jitter. Any experimentally measured histograms of the arrival times bear additionally contributions from the experimental environment [14] via noise in electronics, dispersion in optics and random time difference between laser pulse and reference signal.

### A. Probability density function for the intrinsic jitter

We now estimate expected contributions from different stages in the detection scenario to the intrinsic jitter. According to the original study [19], for statistically independent scattering events the variance (standard deviation) in the quantum yield,  $\sigma N$ , depends on the total deposited energy,  $E$ , and

the mean energy per particle,  $\varepsilon$ , as  $\sigma N = (FE/\varepsilon)^{1/2}$ , where  $F = 0.2\text{--}0.3$  is the Fano factor. For electron avalanche in a superconductor,  $\varepsilon$  equals the superconducting energy gap,  $\Delta$ , while  $E$  is the photon energy,  $h\nu$ , reduced by the additional factor  $\alpha < 1$  which stays for the mean effectiveness of the energy transfer from the photon to electrons. Fluctuations in the quantum yield set the ultimate value of the energy resolution in tunnel-junction photon detectors. Despite extensive efforts this limit has never been achieved [31]. Due to fluctuations of different origins, experimental energy resolution was typically one order of magnitude worse. In our case, the size of the two-dimensional diffusive hot-spot is proportional to its growth time,  $\tau$ , and to the logarithm of the total number of non-thermal electrons,  $N$ . Hence, the variance in the growth time becomes  $\sigma\tau = \tau\sigma N/N = (\alpha F\Delta/(h\nu))^{1/2}$ . With typical parameters of NbN nanowires,  $\sigma\tau/\tau \approx 10^{-3}$  and the variance in the growth time drops below one picosecond even for the largest reported  $\tau \approx 45$  ps [12]. We therefore neglect the contribution from Fano fluctuations in the following consideration.

We also neglect for a while geometric contribution to the intrinsic jitter since measured values of  $\sigma_{\text{int}}$  are noticeably larger than the expected magnitude of the geometric component estimated in Sec. II B. As it will be shown later, the magnitude of the geometric contribution is indeed negligible.

Under the assumptions above the photon count is a combination of only two sequential and statistically independent events: (1) opening of the time window for vortex crossing by the hot-spot and (2) vortex crossing itself. In terms of the probability theory such composite event is described by the probability density function  $h(t) = \int f_1(u)f_2(t-u)du$ , where  $f_1(t)$  and  $f_2(t)$  are PDFs of these two sequential events [20]. Following Gaussian shapes of the left sides (earlier arrival times) of experimental histograms, we assume that the opening time obeys normal distribution with the mean value  $\mu$ , which we set to zero for simplicity, and the variance  $\sigma$ . One of the reasons for statistical distribution of the opening times is the position dependence of the detection current [13,25,26]. The duration of the time window for vortex crossing approximately equals the lifetime of the hot-spot. The value of the lifetime depends on how the borders of the spot are defined. It varies from the electron thermalization time  $\approx 7$  ps [32] through the diffusion time across the nanowire ( $\approx 20$  ps for the 100 nm wire from NbN) to the width of the autocorrelation function (20–45 ps) in two-photon experiments [12]. The PDF of the start time of the vortex crossing is an exponential function with the single characteristic time which represents simultaneously the mean value and the standard deviation. The flight time of the vortex across the nanowire is also statistical variable with the mean value  $\tau_v = \Phi_0(w/\xi)^2(2\pi I_B R_S)^{-1}$ , where  $w$  and  $\xi$  are the width of the wire and the coherence length, respectively, and  $\Phi_0$  is the magnetic flux quantum. With typical NbN parameters the flight time amounts at 12 ps at the experimental critical current. Numerical model [13] predicts the mean flight time of 9 ps. We will not distinguish at this stage between the start time of the crossing and the flight time and approximate both by the single PDF. Following linear slopes of experimental histograms at large delays, we describe probability distribution for the vortex-related delay as an exponential function with the mean value  $\tau_0$ . The PDF

TABLE I. Summary of different contributions to the intrinsic jitter, affecting factors, and favoring experimental techniques.

Jitter origin	Factors affecting jitter		Quantitative description	Experimental approach
	External	Internal		
Geometric		Kinetic inductance, electrical path	Transmission line	Differential readout
	Operational conditions:	Location of the photon absorption:		
Local	<ul style="list-style-type: none"> <li>• temperature,</li> <li>• bias current,</li> <li>• photon energy</li> </ul>	<ul style="list-style-type: none"> <li>• Straight wire</li> <li>• Bend</li> </ul>	<ul style="list-style-type: none"> <li>• Deterministic</li> </ul>	<ul style="list-style-type: none"> <li>Randomness in the grow time of the diffusive hot-spot</li> </ul>
		Detection regime:		Common readout line
		Counting events:		
		<ul style="list-style-type: none"> <li>• Single-photon</li> <li>• Multi-photon</li> </ul>	<ul style="list-style-type: none"> <li>• Probabilistic</li> </ul>	<ul style="list-style-type: none"> <li>Randomness in the start time of vortex crossing</li> </ul>

of the composite event is then the one known as exponentially modified Gaussian distribution,

$$\begin{aligned}
 h(t) &= \int_{-\infty}^t \frac{1}{\sigma\sqrt{2\pi}} \exp\left(-\frac{u^2}{2\sigma^2}\right) \frac{1}{\tau_0} \exp\left(-\frac{t-u}{\tau_0}\right) du \\
 &= \frac{1}{2\tau_0} \exp\left(\frac{1}{2\tau_0}\left(\frac{\sigma^2}{\tau_0} - 2t\right)\right) \cdot \left(1 - \operatorname{erf}\left(\frac{\left(\frac{\sigma^2}{\tau_0} - t\right)}{\sigma\sqrt{2}}\right)\right),
 \end{aligned} \tag{4}$$

where  $\operatorname{erf}(x)$  is the error function. We used Eq. (4) to fit our experimental histograms. Best fits for the  $4 \times 4 \mu\text{m}^2$  meander at wavelengths 800 nm and 1560 nm are shown in Figs. 4(a) and 5(a), respectively. Table II summarizes the best fit parameters for different meanders and wavelengths at three different bias currents.

The exponential distribution is known to be statistically non-stable. This means that formally defined dispersion of the composite PDF (Eq. 4) does not equal the sum of dispersions of the two elementary PDFs. However, we found numerically that the analytical approximation in the form  $(8(\ln 2)\sigma^2 + 4(\ln 2)^2\tau_0^2)^{1/2}$  closely follows FWHM of the composite distribution. This observation verifies our approach for defining intrinsic jitter as FWHM/2.35 of the best fits of the experimental histograms.

Data in Table II show that at the longer wavelength jitter components change only little from meander to meander, although the relative amount of straight wires in the meanders changes by almost one order of magnitude. Furthermore,

random vortex crossing ( $\tau_0$ ) dominates the intrinsic jitter. We have proved earlier that at wavelengths larger than the cut-off, bends in the meander deliver much larger photon count rate than straight portions [29]. Particularly for  $4 \times 4 \mu\text{m}^2$  meander, the spectral cut-off in the detection efficiency at  $I_B = 0.95 I_C$  occurs around the wavelength 600 nm [25]. All together these observations evidence that at the longer wavelength bends dominate jitter and that they detect photons in the probabilistic regime.

At the shorter wavelength and at the larger current, contributions to the local jitter from the appearance of the hot-spot ( $\sigma$ ) and from the vortex crossing ( $\tau_0$ ) are close. Contributions to the jitter from both processes increase when the relative amount of bends in the total length of the meandering wire increases. We therefore suppose that detection events in the smaller meander are dominated by bends which provide larger jitter than the detection events in straight wires. Contrarily, in the larger meander, the count rate and jitter are dominated by the detection events in straight wires. Data from Table II do not suffice to conclude on the detection regime in bends or straight wires at the shorter wavelength.

### B. Local jitter: Bends and straight wires

In a further attempt to separate counts arriving from bends and straight wires, we geometrically divide each meander into two parts. The part with bends has the length  $L_b = n(2w + s)$ , where  $s$  is the separation between wires and  $n$  the number of bends. The part with straight wires has total length  $L - L_b$ ,

TABLE II. Best fit parameters for fits of experimental histograms (probability density functions) with Eq. (4).

	$I_B/I_C$	Fitting parameter (ps)	Meander size ( $\mu\text{m}^2$ )			
			$4 \times 4$	$4 \times 3$	$4 \times 2$	$4 \times 1$
800 nm	0.95	$\sigma$	$5.25 \pm 0.07$	$5.9 \pm 0.18$	$6.53 \pm 0.06$	$10 \pm 0.1$
		$\tau_0$	$5.3 \pm 0.16$	$5.67 \pm 0.08$	$8.66 \pm 0.13$	$11.7 \pm 0.3$
	0.8	$\sigma$	$10.2 \pm 0.22$	$8.8 \pm 0.16$	$9.29 \pm 0.14$	$9.3 \pm 0.28$
		$\tau_0$	$11.54 \pm 0.55$	$11.8 \pm 0.36$	$11.7 \pm 0.3$	$10.7 \pm 0.63$
1560 nm	0.95	$\sigma$	$13 \pm 0.16$	$15 \pm 0.45$	$15 \pm 0.3$	$14.7 \pm 0.4$
		$\tau_0$	$23 \pm 0.5$	$22.5 \pm 0.6$	$23 \pm 0.6$	$22 \pm 0.9$
	0.7	$\sigma$	$14.96 \pm 0.16$	$15 \pm 0.45$		$15 \pm 0.45$
		$\tau_0$	$16.37 \pm 0.5$	$18 \pm 0.5$		$20.6 \pm 0.6$

where  $L$  is the total length of the meandering wire. Photon counts coming from bends and straights are mutually exclusive independent events and the probability of either to occur is the sum of the probabilities of their occurrences taken with corresponding geometric weights  $G = L_b/L$  and  $1 - G$ . For our larger meanders  $G = 0.025$ . The dispersion for two mutually exclusive events is the sum of dispersions of elementary events. According to Eq. (3), intrinsic timing jitter contains statistically independent contributions from local and geometric jitters. We present local jitter as containing statistically independent contributions from bends,  $\sigma_{\text{bend}}$ , and from straight wires,  $\sigma_{\text{wire}}$ . Considering the nanowire as a portion of a transmission line, we present geometric jitter as  $L/k$ , where  $k$  plays the role of the effective propagation velocity of electric transients. Equation (3) can be now rewritten to obtain

$$\sigma_{\text{int}}^2 = G \sigma_{\text{bend}}^2 + (1 - G) \sigma_{\text{wire}}^2 + (L/k)^2. \quad (5)$$

Writing down this equation for each meander, we obtain a system of four equations with three unknown independent variables  $\sigma_{\text{bend}}$ ,  $\sigma_{\text{wire}}$ , and  $k$ . For each bias current and wavelength, we found solutions of four possible different systems each containing three equations from the set of four. We then computed the mean value out of four solutions for each independent variable. For  $\sigma_{\text{wire}}$  and  $\sigma_{\text{bend}}$ , the procedure delivers the accuracy better than 12%. Parameter  $G$  was assumed to be current independent. We verified that changing this parameter leads to minor changes in absolute values of  $\sigma_{\text{wire}}$  and  $\sigma_{\text{bend}}$  but does not affect their current dependencies. The solution for the wavelength 800 nm and  $I_B = 0.95 I_C$  delivers the effective propagation velocity  $k = 70 \mu\text{m}/\text{ps}$  and the geometric jitter varying between 0.3 and 1.17 ps for meanders from  $4 \times 1 \mu\text{m}^2$  to  $4 \times 4 \mu\text{m}^2$ , correspondingly. This value of the effective velocity is approximately one half of the expected propagation velocity ( $\approx 140 \mu\text{m}/\text{ps}$ ) for a metallic coplanar line on sapphire but more than one order of magnitude larger than the expected propagation velocity through our superconducting meander line [16]. This result confirms our supposition that the geometric jitter is effectively eliminated in our experimental configuration. Since the geometric contribution is much smaller than any measured value of the intrinsic jitter, we neglected geometric jitter in the following consideration.

We have to admit that the contributions to the jitter from bends and straight wires are additionally weighted with the local detection probabilities. Anyway, for the larger meander, the detection efficiency at  $I_B = 0.95 I_C$  and 800 nm is 20% from the saturated detection efficiency [27]. This is still one order of magnitude larger than the relative amount of bends. Hence, we are confident that at our operational conditions straight wires dominate the count rate in the larger meander.

Figure 6 shows current dependencies of the jitter for events originating from bends and wires at two wavelengths. Jitter from bends grows monotonously with the current at both wavelengths. Jitter from straight wires behaves differently. It demonstrates monotonous growth with the current only at the longer wavelength. At shorter wavelengths, sharp decrease replaces at large currents monotonous growth which is seen at small currents. In the next section, we show that different current dependencies correspond to different detection regimes.

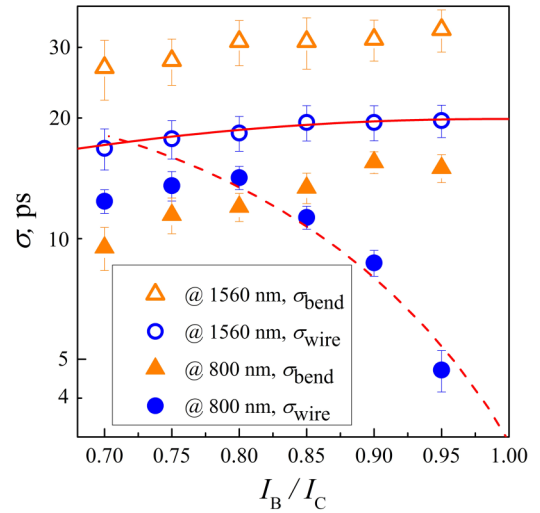


FIG. 6. Contributions to the local jitter from bends (triangles) and wires (circles) vs. relative current. Open and closed symbols correspond to wavelengths 1560 and 800 nm, respectively. Lines show best fits to experimental data obtained with Eq. (7) (solid line) and Eq. (6) (dashed line). The error bars denote the uncertainties of which result from solving system containing Eq. (5) for all four meanders.

### C. Current dependencies of the jitter for deterministic and probabilistic regimes

Experimental results presented in Figs. 4 and 5 show that the histograms become almost symmetric and Gaussian when the meanders enter deterministic detection regime (large current, short wavelength) and that they exhibit large exponential tail when meanders detect probabilistically (long wavelength). In terms of the composite PDF of Eq. (4), probabilistic regime corresponds to  $\sigma < \tau_0$  while in the deterministic regime  $\sigma \geq \tau_0$ . We invoke position dependence of the detection current across the nanowire [25] to model current dependence of the intrinsic jitter in the deterministic regime. The authors of Ref. [25] showed that due to current crowding the detection current,  $I_{\text{det}}$ , depends on the hot-spot position across the nanowire. The detection current reaches the maximum in the middle of the wire and drops to symmetric minima which are located near both edges of the wire. We denote corresponding values of the detection current as  $I_{\text{det}}^{\text{max}}$  and  $I_{\text{det}}^{\text{min}}$ . The detection criterion is fulfilled when the velocity of superconducting electrons reaches the critical value. This occurrence initiates vortex crossing. Although at  $I_B > I_{\text{det}}^{\text{max}}$  the whole wire responds deterministically, the size of the hot-spot needed to initiate vortex crossing is different at different locations. It is larger in the middle of the wire and goes to minima close to wire edges. At  $I_B < I_{\text{det}}^{\text{min}}$  detection criterion is not reached and the wire responds probabilistically. At intermediate currents, only that part of the wire where  $I_{\text{det}} < I_B$  responds deterministically. As it has been discussed above, the size of the hot-spot is largely undefined. Here we use the model of the diffusive normal core [18] to connect the local detection current and the radius of the spot,  $R$ , as  $(1 - I_{\text{det}}/I_{\text{dep}}) = 2R/w$ , where  $I_{\text{dep}}$  is the depairing current. The spot grows due to diffusion and reaches the radius  $R$  after a time  $\tau_D = R^2/4D$  where  $D$  is the diffusion coefficient.

This time represents the time delay between photon absorption and the deterministic vortex crossing. We further associate the standard deviation  $\delta\tau$  in this time with the difference between diffusion times corresponding to the maximum and the minimum values of the detection current to obtain

$$\delta\tau = \eta^2 \frac{w^2}{16D} \left\{ \left(1 - I_{\text{det}}^{\text{min}}/I_{\text{dep}}\right)^2 - \left(1 - I_{\text{det}}^{\text{max}}/I_{\text{dep}}\right)^2 \right\}. \quad (6)$$

The coefficient  $\eta$  will be used as a fit parameter. It accounts for uncertainty of the effective hot-spot size which is relevant to our experiment. This effective size may differ from the one defined in the model of the diffusive normal-core [18]. We used the output of numerical calculations [25] to find the values of  $I_{\text{det}}^{\text{max}}$  and  $I_{\text{det}}^{\text{min}}$  at different mean values, which we associated with applied bias current, and computed the standard deviation. Figure 6 shows the best fit of the current dependence of  $\sigma_{\text{wire}}$  at 800 nm. It was obtained with Eq. (6) for  $I_C/I_{\text{dep}} = 0.88$  and  $\eta = 2.2$ . This value shows that the size of the hot-spot, which is relevant for our experiment, is approximately twice as large as the size predicted by the diffusive core approximation. We have to note that Gaussian shape of PDFs which was found in the experiment cannot be explained in the framework of our model. The most plausible reason is that the connection between local detection current and the size of the hot-spot may also depend on the spot location. The approach of the energy barrier for vortex entry fails to reproduce Gaussian PDFs, which we obtained in the experiment.

If the deterministic detection criterion is not reached, the wire may respond probabilistically. In this case the vortex crossing occurs within the lifetime of the hot-spot,  $\tau_{\text{HS}}$ . The delay between the spot appearance and the start time of crossing is described by exponential PDF with the mean rate  $p = \tau_V^{-1} \exp[-U(I_B)/kT]$ , where  $U(I_B)$  is the current dependent instantaneous barrier for vortex entry and  $\tau_V \propto I_B^{-1}$  is the time it takes for the vortex to cross the wire in the absence of the barrier. Such statistics is typical for any system escaping from a metastable state over potential barrier [22,30]. For NbN wires studied here,  $\tau_V(I_C) = 12$  ps. Because of the small size of the hot-spot as compared to the wire width, change in the barrier  $U$  during the time  $\tau_{\text{HS}}$  is not uniform across the width. We simplified the approach by taking the expression for the current dependence of the barrier  $U(I_B)$  with the uniform free energy (Eq. (4) from Ref. [21]) and use the energy scale  $\varepsilon_0$  as fitting parameter. In the framework of this approximation, the standard deviation in the delay time takes the form

$$\delta\tau = \int_0^{\tau_{\text{HS}}} (t - \langle\tau\rangle)^2 p e^{-p t} dt, \quad (7)$$

where the mean value  $\langle\tau\rangle$  is defined with the same PDF within the lifetime of the hot-spot. Best fit of the current dependence of  $\sigma_{\text{wire}}$  at 800 nm with the Eq. (7) is shown in Fig. 6. It was obtained with  $\tau_{\text{HS}} = 65$  ps and the value of  $\varepsilon_0$  equal to 0.6% of its equilibrium value at the ambient temperature. In

the framework of our simplified model, this very small best fit value of the effective vortex energy compensates for the lack of numerical accuracy of the theory with uniform suppression of the free energy [22]. The best fit value of the lifetime is slightly larger than the lifetime 45 ps [12] concluded from correlation measurements. However, this can be a coincidence since the spot size is defined differently in different experiments. The best fit value of  $\tau_{\text{HS}}$  translates into the spot size close to the hot-spot size resulted from the best fit in the deterministic regime. Hence, the same size of the hot-spot matters for two sequential events building the composite PDF. This similarity indicates plausibly the self-consistence of our interpretation.

The fact that Eqs. (6) and (7) fit very accurately our experimental data justifies our interpretation of two different contributions to the local jitter as contributions from deterministic and probabilistic events. This is especially sound for straight wires where the change from probabilistic to deterministic regime with the increase in the current is clearly seen. The current dependence of  $\sigma_{\text{bend}}$  at 800 nm is similar to current dependencies of  $\sigma_{\text{wire}}$  and  $\sigma_{\text{bend}}$  at 1560 nm where they both detect probabilistically. We therefore argue that bends detect photons probabilistically also at 800 nm. The reason is that the difference between  $I_{\text{det}}^{\text{max}}$  and  $I_{\text{det}}^{\text{min}}$  in bends is much larger than in wires [29] and true deterministic regime for bends cannot be realized within available range of bias currents.

## V. CONCLUSION

Studying current dependencies of timing jitter in photon counts delivered by meandering nanowires, we have found that asymmetry of histograms representing jitter as well as its value and current dependencies differ drastically at two different photon energies. By analyzing statistics in appearance times of photon counts, we have shown that each count is a composite event including at least two elementary events described by Gaussian and exponential distributions of probability densities. We associated these events with the growth of the hot-spot and consequent jump of a magnetic vortex across the wire. We have found that at the lower photon energy exponential distribution due to vortex jumps dominates the jitter.

We have related probabilistic and deterministic detection regimes in the spectrum of the photon count rate to the dominance of either vortex crossing or the hot-spot growth in the measured jitter, respectively. Invoking varying geometric weights of bends and straights in studied meanders, we have separated contributions from bends and wires to the measured jitter and have shown that bends respond probabilistically at both photon energies while straights undergo deterministic regime at the higher photon energy.

Finally, we have proposed simplified but analytical models that describe experimentally observed current dependencies of timing jitter in bends and straight wires at different photon energies.

[1] Lixing You, Xiaoyan Yang, Yuhao He, Wenxing Zhang, Dengkuan Liu, Weijun Zhang, Lu Zhang, Ling Zhang, Xiaoyu Liu, Sijing Chen, Zhen Wang, and

Xiaoming Xie, Jitter analysis of a superconducting nanowire single photon detector, *AIP Adv.* **3**, 072135 (2013).

- [2] V. Shcheslavskiy, P. Morozov, A. Divochiy, Yu. Vakhtomin, K. Smirnov, and W. Becker, Ultrafast time measurements by time-correlated single photon counting coupled with superconducting single-photon detector, *Rev. Sci. Instrum.* **87**, 053117 (2016).
- [3] Q. Zhao, L. Zhang, T. Jia, L. Kang, W. Xu, J. Chen, and P. Wu, Intrinsic timing jitter of superconducting nanowire single-photon detectors, *Appl. Phys. B* **104**, 673 (2011).
- [4] N. Calandri, Qing-Yuan Zhao, Di Zhu, A. Dane, and Karl K. Berggren, Superconducting nanowire detector jitter limited by detector geometry, *Appl. Phys. Lett.* **109**, 152601 (2016).
- [5] Maria V. Sidorova, Alexander V. Divochiy, Yury B. Vakhtomin, and Konstantin V. Smirnov, Ultrafast superconducting single-photon detector with a reduced active area coupled to a tapered lensed single-mode fiber, *J. Nanophotonics* **9**, 093051 (2015).
- [6] J. A. O'Connor, M. G. Tanner, C. M. Natarajan, G. S. Buller, R. J. Warburton, S. Miki, Z. Wang, S. W. Nam, and R. H. Hadfield, Spatial dependence of output pulse delay in a niobium nitride nanowire superconducting single-photon detector, *Appl. Phys. Lett.* **98**, 201116 (2011).
- [7] V. B. Verma, B. Korzh, F. Bussi eres, R. D. Horansky, A. E. Lita, F. Marsili, M. D. Shaw, H. Zbinden, R. P. Mirin, and S. W. Nam, High-efficiency WSi superconducting nanowire single-photon detectors operating at 2.5 K, *Appl. Phys. Lett.* **105**, 122601 (2014).
- [8] Yu. P. Korneeva, M. Yu. Mikhailov, Yu. P. Pershin, N. N. Manova, A. V. Divochiy, Yu. B. Vakhtomin, A. A. Korneev, K. V. Smirnov, A. G. Sivakov, A. Yu. Devizenko, and G. N. Goltsman, Superconducting single-photon detector made of MoSi film, *Supercond. Sci. Technol.* **27**, 095012 (2014).
- [9] A. G. Kozorezov, C. Lambert, F. Marsili, M. J. Stevens, V. B. Verma, J. P. Allmaras, M. D. Shaw, R. P. Mirin, and Sae Woo Nam, Fano fluctuations in superconducting nanowire single-photon detectors, *Phys. Rev. B* **96**, 054507 (2017).
- [10] J. Zhang, W. Slys, A. Pearlman, A. Verevkin, R. Sobolewski, O. Okunev, G. Chulkova, and G. N. Gol'tsman, Time delay of resistive-state formation in superconducting stripes excited by single optical photons, *Phys. Rev. B* **67**, 132508 (2003).
- [11] K. Harrabi and J. P. Maneval, Measurements of the delay time between a critical current pulse and the first resistive response in superconducting niobium strips, *IEEE Trans. Appl. Supercond.* **27**, 2201104 (2017).
- [12] S. Ferrari *et al.*, Hot-spot relaxation time current dependence in niobium nitride waveguide-integrated superconducting nanowire single-photon detectors, *Opt. Express* **25**, 8739 (2017).
- [13] Hao Wu, Chao Gu, Yuhao Cheng, and Xiaolong Hu, Vortex-crossing-induced timing jitter of superconducting nanowire single-photon detectors, *Appl. Phys. Lett.* **111**, 062603 (2017).
- [14] Junjie Wu, Lixing You, Sijing Chen, Hao Li, Yuhao He, Chaolin Li, Zhen Wang, and Xiaoming Xie, Improving the timing jitter of a superconducting nanowire single-photon detection system, *Appl. Opt.* **56**, 2195 (2017).
- [15] A. Semenov, P. Haas, B. G unther, H.-W. H ubers, K. Ilin, M. Siegel, A. Kirste, J. Beyer, D. Drung, and T. Schurig, Energy resolution and sensitivity of a superconducting quantum detector, *Physica C* **460–462**, 1491 (2007).
- [16] Daniel F. Santavica, Jesse K. Adams, Lierd E. Grant, Adam N. McCaughan, and Karl K. Berggren, Microwave dynamics of high aspect ratio superconducting nanowires studied using self-resonance, *J. Appl. Phys.* **119**, 234302 (2016).
- [17] F. Najafi, Superconducting nanowire single-photon detectors: new detector architectures and integration with photonic chips, Ph.D. thesis, Massachusetts Institute of Technology, 2015.
- [18] Alex D. Semenov, Gregory N. Gol'tsman, and Alexander A. Korneev, Quantum detection by current carrying superconducting film, *Physica C* **351**, 349 (2001).
- [19] U. Fano, Ionization yield of radiations. II. The fluctuations of the number of ions, *Phys. Rev.* **72**, 26 (1947).
- [20] V. E. Gmurman, *Fundamentals of Probability Theory and Mathematical Statistics*, edited by I. I. Berenblut (Iiffe Books Limited, UK, 1968).
- [21] M. Hofherr, D. Rall, K. Ilin, M. Siegel, A. Semenov, H.-W. H ubers, and N. A. Gippius, Intrinsic detection efficiency of superconducting nanowire single-photon detectors with different thicknesses, *J. Appl. Phys.* **108**, 014507 (2010).
- [22] L. N. Bulaevskii, Matthias J. Graf, and V. G. Kogan, Vortex-assisted photon counts and their magnetic field dependence in single-photon superconducting detectors, *Phys. Rev. B* **85**, 014505 (2012).
- [23] A. N. Zotova and D. Y. Vodolazov, Photon detection by current-carrying superconducting film: A time-dependent Ginzburg-Landau approach, *Phys. Rev. B* **85**, 024509 (2012).
- [24] J. J. Renema, Q. Wang, R. Gaudio, I. Komen, K. op't Hoog, D. Sahin, A. Schilling, M. P. van Exter, A. Fiore, A. Engel, and M. J. A. de Dood, Position-dependent local detection efficiency in a nanowire superconducting single-photon detector, *Nano Lett.* **15**, 4541 (2015).
- [25] A. N. Zotova and D. Yu. Vodolazov, Intrinsic detection efficiency of superconducting nanowire single photon detector in the modified hot spot model, *Supercond. Sci. Technol.* **27**, 125001 (2014).
- [26] A. Engel, J. Lonsky, X. Zhang, and A. Schilling, Detection mechanism in SNSPD: Numerical results of a conceptually simple, yet powerful detection model, *IEEE Trans. Appl. Supercond.* **25**, 2200407 (2015).
- [27] I. Charaev, A. Semenov, S. Doerner, G. Gomard, K. Ilin, and M. Siegel, Current dependence of the hot-spot response spectrum of superconducting single-photon detectors with different layouts, *Supercond. Sci. Technol.* **30**, 025016 (2017).
- [28] D. Yu. Vodolazov, Current dependence of the red boundary of superconducting single-photon detectors in the modified hot-spot model, *Phys. Rev. B* **90**, 054515 (2014).
- [29] A. Semenov, I. Charaev, R. Lusche, K. Ilin, M. Siegel, H.-W. H ubers, N. Bralovi c, K. Dopf, and D. Yu. Vodolazov, Asymmetry in the effect of magnetic field on photon detection and dark counts in bended nanostraps, *Phys. Rev. B* **92**, 174518 (2015).
- [30] P. Hanggi, Escape from a metastable state, *J. Stat. Phys.* **42**, 105 (1968).
- [31] P. Lerch and A. Zender, *Quantum Giaever Detectors: STJ's*, edited by Chr. Enss, Cryogenic Particle Detection, Applied Physics (Springer, Berlin/Heidelberg, 2005), Vol. 99, pp. 217–267.
- [32] K. S. Ilin, M. Lindgren, M. Currie, A. D. Semenov, G. N. Gol'tsman, R. Sobolewski, S. I. Cherednichenko, and E. M. Gershenzon, Picosecond hot-electron energy relaxation in NbN superconducting photodetectors, *Appl. Phys. Lett.* **76**, 2752 (2000).